

Research Article

Dynamic Analysis of Flexible Shaft and Elastic Disk Rotor System Based on the Effect of Alford Force

Wenjun Yang ^{1,2}, Huiqun Yuan ³, Li Hui,² and Kaifeng Zhang⁴

¹School of Mechatronics Engineering, Shenyang Aerospace University, Shenyang, China

²State Key Laboratory for Aviation Digital Manufacturing Process, Shenyang Aerospace University, Shenyang, China

³College of Science, Northeastern University, Shenyang, China

⁴School of Mechatronics Engineering, Shenyang Aerospace University, Shenyang, China

Correspondence should be addressed to Wenjun Yang; ncywj@163.com

Received 24 October 2018; Accepted 9 December 2018; Published 14 February 2019

Academic Editor: Jussi Sopanen

Copyright © 2019 Wenjun Yang et al. This is an open access article distributed under the Creative Commons Attribution License, which permits unrestricted use, distribution, and reproduction in any medium, provided the original work is properly cited.

Taken the flexible shaft and elastic disk rotor system as the research object, vibration differential equations are established by the modal synthesis method. Based on the Runge–Kutta method of direct integration, dynamic equations are solved successfully. Then, the effects of Alford force caused by the airflow excitation are researched on the stability and dynamic response. The results show modal vibration of the disk takes a great effect on the coupled natural frequency of shaft transverse vibration in the high rotational speed region. The effect of shaft-disk coupling makes rotor frequency to decrease, and different rotational speeds have little effect on rotor frequency. Eccentric distance is sensitive to the amplitude of rotor response, but it has little effect on rotor stability, motion law, and relative relationship of two response frequencies. The proportion of rotor responses caused by aerodynamic excitation force becomes larger with the increase of rotational speed and disk radius. However, the proportion decreases with the second support moving to the right, and it is helpful for the stable operation of the rotor system.

1. Introduction

As a kind of large rotating machinery, a gas turbine is widely applied in industrial fields such as aviation, aerospace, transportation, and electric power. It takes an important role in national economy.

A gas turbine works under the high-speed environment, and various nonlinear factors are shown on strong coupling, high dimension, and unsteady state. There will be hidden serious problems in operation, and it is often huge and even disastrous if the accidents occur.

For a discontinuous system of the mass continuous distribution axis, it is difficult to express the dynamic characteristics of all parts in an equation. Gao and Meng [1] studied the vibration and stability characteristics of elastically supported cantilever beam by the transfer matrix method. But, this research was only on a continuous beam and shaft

system, the effect of the disk was neglected on dynamic characteristics. By combining the modal synthesis method with the transfer matrix method, Han et al. [2] solved the dynamic characteristics of a complex rotor system.

With the appearance of optimization design techniques, the rotor structure is continuously improved. The wheel disk is made much thinner so that coupling vibration is more obvious between blade and disk. So elastic disk modeling is very important for the research on the gas turbine disk-shaft system. Zhang [3] established the perturbation motion equation of the flexible shaft-elastic disk rotor. Based on the finite element method, Meek et al. [4, 5] analyzed the dynamic characteristics of a rigid disc-flexible shaft rotor system. Hili et al. [6] developed an elastic disk-rigid shaft model with an elastic support, and the effects of elastic deformation and elastic support are discussed on rotor responses when the disk is under axial load.

In addition, fluid-solid coupling problems affect rotor stable operation seriously. It easily leads to the instability phenomenon by airflow excitation in gas turbine working [7, 8]. Because there is always the relative eccentricity between rotor blade and casing, the clearance of the blade tip is unevenly distributed along the circumferential direction. This makes the distributions of blade efficiency, pressure, and aerodynamic force different.

So except for a torque, blade circumferential aerodynamic force is also combined with Alford force, which is acting on the axis and perpendicular to eccentric shifting [9]. Alford force is a cyclic force. Once it is larger than the external damping to maintain the system stable, positive work will be performed on the rotor system. That is inputting energy to promote the development of rotor whirl motion. The self-excited vibration will occur when its amplitude increases continuously.

A steam turbine was made by GE corporation, and a strong fluid gap vibration was produced when the load was increased [10]. This is the first time that the phenomenon of aerodynamic excitation was discovered in a rotating machine. Soon after, Thomas also reported a similar vibration phenomenon [11]. He first proposed the concept of gap excitation and suggested the calculation formula for turbine gap excitation force. However, the problem did not attract enough attention at that time.

In 1957, the first ultra-supercritical pressure units were operated at American Ohio Ferrer Power Plant. After that, the former Soviet Union, West Germany, and Japan had also developed and taken into operation the ultra-supercritical pressure units. In working operation, there are quite a few aerodynamic excitation problems on several supercritical units. Because of the higher steam parameters, aerodynamic excitation of a high-pressure rotor is increased on high-power ultra-supercritical pressure units.

In the 1960s, the problem of aerodynamic excitation occurred again. At this period, the gap excitation mainly took place in the turbine of high-power ultra-supercritical pressure units which were manufactured by the Federal Republic of Germany. In the study of aeroengines stability, American scholar J. S. Alford achieved the important progress in theory. In his research, the theory of gap-flow excitation was proposed for the first time, and the calculation formula of turbine excitation force was given. Then, the problem of gap excitation was given enough attention.

For experimental verification of Alford's force, Urlichs and Wohkab [12, 13], respectively, developed the experimental research on turbine engines. Vance and Laudadio [14] performed the test of lateral force acting on the blower impeller and confirmed the presence of Alford force. In the sealing force models proposed by Thomas and Alford, circumferential flow velocity is ignored at the inlet, which is the primary factor of crosscut forces.

Soviet scholars studied the spiral effect of aerodynamic flow in a high-pressure turbine rotor and found that the inertial effect of aerodynamic flow is far greater than the friction effect in the sealing gap [15]. At the end of the twentieth century, more researchers began to study

aerodynamic excitation forces and the interaction forces between impeller and flow section [16, 17]. Shanghai Power Equipment Research Institute conducted an experiment on the aerodynamic oscillation of a gas turbine [18]. Considering the excitation of aerodynamic force, a small-scale modeling test rig was established by the single-span flexible rotor. Then, a simplified calculation method was proposed for the airflow excitation stiffness. The stability and unstable rotation speed were analyzed on the 200 MW turbine power generators.

Chai et al. [19] developed a further research on the airflow exciting force. Taken from the fluid dynamics, the Alford force formula of the uniform flow field was derived on a straight blade and a twisted blade. Chen and Sun [20] proposed an entirely new method of oscillatory fluid dynamics, and it was used for solving the airflow stability and dynamic coefficient of air seal.

Lu et al. [21] analyzed aerodynamic excitation in the cylinder of 200 MW high-pressure turbine and discussed the effect of aerodynamic excitation on the stability of the rotor system. For modifying the formula of Alford force, Yang et al. [22] decomposed rotor displacement into static displacement and dynamic displacement. This provided a method for adjusting rotor static displacement to reduce the exciting force.

In this paper, vibration differential equations of an elastic disk-flexible shaft rotor are established by the modal synthesis method. Based on the Runge-Kutta method of direct integration, dynamic equations are solved successfully. Then, the effects of Alford force caused by the airflow excitation are researched on the stability and dynamic response.

2. Vibration Characteristics of Disk-Shaft Coupling System

Figure 1 is the model of the elastic disk with inner diameter a and outer diameter b . For keeping the disk orthogonal to the shaft in all modes, it is assumed that the contact between disk and shaft is rigid. The differential equation of transverse elastic vibration can be derived by Hamilton's principle. The free vibration equation of the disk is expressed as

$$\rho_D h_D \frac{\partial^2 u_D}{\partial t^2} + D \nabla^4 u_D - \frac{1}{r} \frac{\partial}{\partial r} \left(r N_r \frac{\partial u_D}{\partial r} \right) - \frac{1}{r^2} N_\theta \frac{\partial^2 u_D}{\partial \theta^2} = 0. \quad (1)$$

In order to simulate dynamic characteristics of a flexible shaft and an elastic disk rotor system, the elastic circular plate with an inner clamp edge and outer freedom edge is adopted in the research.

Bending displacement of the elastic disk is expressed as

$$u_D(r, \theta, t) = \sum_{i=1}^{\infty} U_i(r, \theta) q_i(t), \quad (2)$$

where $U_i(r, \theta)$ is the orthogonal mode of the disk and $q_i(t)$ is the time-related part of generalized coordinates. Here, it is

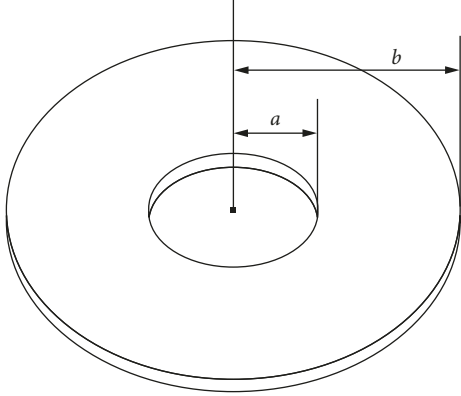


FIGURE 1: Schematic diagram of the disk.

the simple harmonic vibration, so $\ddot{q}_i(t) = -\omega_i^2 q_i(t)$, where ω_i is the i -order natural frequency of the elastic disk. $U_i(r, \theta)$ can be expressed as

$$U_i(r, \theta) = U_{mn}(r, \theta) = R_{mn}(r)(a_{mn} \cos m\theta + b_{mn} \sin m\theta),$$

$$m, n = 0, 1, \dots, \infty, \quad (3)$$

where U_{mn} is indicated as the orthogonal mode with m nodal diameters and n circles. $U_i(r, \theta)$ can be expressed as U_{mn} by the reordering of natural frequencies increasing. $R_{mn}(r)$ is the radial distribution of mode shapes; a_{mn} and b_{mn} are constants which determine the initial angle of the disk combined mode.

For a full symmetric disk, theoretical analysis and experiments have shown there is no fixed initial angle for the disk mode whether it is uniform or not. To simplify the following formula, it is generally assumed that the initial angle is zero. When boundary conditions are certain, $R_{mn}(r)$ has the inherent form.

Inertia force of the vibrating disk is expressed as

$$F_p = -\rho_D h_D \sum_{i=1}^{\infty} \omega_i^2 q_i(t) \int_0^{2\pi} \int_a^b R_{mn}(r) \cos(m\theta) r dr d\theta. \quad (4)$$

In the formula,

$$\int_0^{2\pi} \cos(m\theta) d\theta = \begin{cases} 2\pi, & m = 0, \\ 0, & m \neq 0. \end{cases} \quad (5)$$

The direction of inertia moment at p point is perpendicular to the axis. It is expressed as

$$M_p = -\rho_D h_D \sum_{i=1}^{\infty} \omega_i^2 q_i(t) \int_0^{2\pi} \int_a^b R_{mn}(r) \cos(m\theta) \cos \theta r^2 dr d\theta. \quad (6)$$

In the formula,

$$\int_0^{2\pi} \cos(m\theta) \cos \theta d\theta = \begin{cases} \pi, & m = 1, \\ 0, & m \neq 1. \end{cases} \quad (7)$$

From equations (4) and (6), it can be found that the zero-diameter mode of the disk is coupled with longitudinal

vibration of the shaft by the effect of inertia force F_p . In addition, one pitch diameter mode of the disk is coupled with bending vibration of the shaft by the effect of inertia moment. However, other pitch diameter modes of the disk are not coupled with bending vibration of the shaft. So the bending coupled vibration is only discussed, and one pitch diameter mode of the disk is selected.

3. Dynamic Modeling of Flexible Shaft and Elastic Disk Rotor System

3.1. Rotor Dynamics Model of Flexible Shaft and Elastic Disk.

The model of the flexible disk-flexible rotor system is shown in Figure 2. The disk is located at the leftmost end of the shaft. The distance from the first spring support to the disc is l_1 , the distance between the two spring supports is l_2 , and the distance from shaft end to the second spring support is l_3 .

For describing motion state of the shaft, four variables v_{s1} , w_{s1} and v_{s2} , w_{s2} are taken in two planes which are relatively vertical. Among them, v_{s1} and w_{s1} indicate small lateral deformation by the effect of bending, and v_{s2} and w_{s2} indicate small lateral deformation by the effect of shearing. Therefore, total deformation of the shaft is expressed as

$$\begin{aligned} v_s &= v_{s1} + v_{s2}, \\ w_s &= w_{s1} + w_{s2}. \end{aligned} \quad (8)$$

In the rotating coordinate system, potential energy of the shaft due to bending and shearing can be expressed as

$$\begin{aligned} V_s &= \frac{1}{2} \int_0^S \left\{ kG_s A_s \left[\left(\frac{\partial v_{s2}}{\partial x} \right)^2 + \left(\frac{\partial w_{s2}}{\partial x} \right)^2 \right] \right. \\ &\quad \left. + E_s I_s \left[\left(\frac{\partial^2 v_{s1}}{\partial x^2} \right)^2 + \left(\frac{\partial^2 w_{s1}}{\partial x^2} \right)^2 \right] \right\} dx, \end{aligned} \quad (9)$$

where k is the shape factor which is a constant related to the shaft cross-sectional shape. It can characterize the distribution of uneven shear stress in the cross-sectional area. E_s , G_s , and A_s are axis Young's modulus, shear mode, and cross-sectional area, respectively. I_s is the axis inertia moment related to diameter.

Due to translation and rotation, kinetic energy of the axis can be expressed as

$$\begin{aligned} T_s &= \frac{1}{2} \int_0^S \rho_s A_s \left[\dot{v}_s^2 + \dot{w}_s^2 + 2\Omega(\dot{w}_s v_s - w_s \dot{v}_s) + \Omega^2(v_s^2 + w_s^2) \right] dx \\ &\quad + \frac{1}{2} \int_0^S \rho_s I_s \left[\dot{\theta}_{s\xi}^2 + \dot{\theta}_{s\eta}^2 + 2\Omega(\dot{\theta}_{s\xi} \theta_{s\eta} + \theta_{s\xi} \dot{\theta}_{s\eta}) - \Omega^2(\theta_{s\xi}^2 + \theta_{s\eta}^2) \right] dx \\ &\quad + \int_0^S \rho_s I_s \Omega^2 dx, \end{aligned} \quad (10)$$

where ρ_s is the density of the shaft. $\theta_{s\xi}$ and $\theta_{s\eta}$ denote the small-angle rotation of the shaft cross section due to bending, and they can be expressed as

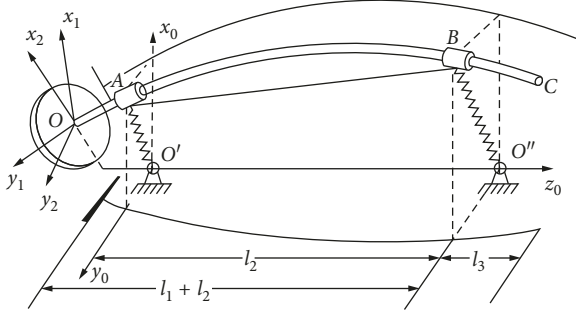


FIGURE 2: Rotor model of the flexible shaft and the elastic disk.

$$\begin{aligned}\theta_{s\xi} &= -\frac{\partial w_{s1}}{\partial x}, \\ \theta_{s\eta} &= \frac{\partial v_{s1}}{\partial x}.\end{aligned}\quad (11)$$

Kinetic energy of the disk is expressed as

$$\begin{aligned}T_D &= \frac{1}{2}m_D[\dot{v}^2 + \dot{w}^2 + 2\Omega(\dot{w}v - v\dot{w}) + \Omega^2(v^2 + w^2)] \\ &+ \frac{1}{2}J_{Dy}[(\dot{\theta}_\xi - \Omega\theta_\eta)^2 + (\dot{\theta}_\eta + \Omega\theta_\xi)^2] \\ &+ \frac{1}{2}J_{Dx}[2\Omega\theta_\eta\dot{\theta}_\xi - \Omega^2(\theta_\xi^2 + \theta_\eta^2) + \Omega^2] \\ &+ \frac{1}{2}\rho_D h_D \int_0^{2\pi} \int_a^b \{ \dot{u}_D^2 + 2r[\sin\theta(\dot{\theta}_\xi - \Omega\theta_\eta) \\ &- \cos\theta(\dot{\theta}_\eta + \Omega\theta_\xi)]\dot{u}_D \} - 2\Omega r[\sin\theta(\dot{\theta}_\eta + \Omega\theta_\xi) \\ &+ \cos\theta(\dot{\theta}_\xi - \Omega\theta_\eta)]\dot{u}_D \} r dr d\theta,\end{aligned}\quad (12)$$

where m_D is the mass of the disk, J_{Dx} and J_{Dy} are the disc inertia moments of axis and radial direction, v and w are the shaft displacements at the disc location, and θ_ξ and θ_η denote the small rotation angle caused by shaft bending. The tiny rotation angle is ignored which is caused by the rigid body displacements because it will be eliminated in the Lagrangian equation.

Strain energy of the disk can be expressed as

$$\begin{aligned}V_D &= \frac{D}{2} \int_0^{2\pi} \int_a^b \left\{ (\nabla^2 u_D)^2 - 2(1-\nu_D) \frac{\partial^2 u_D}{\partial r^2} \left(\frac{1}{r} \frac{\partial u_D}{\partial r} + \frac{1}{r^2} \frac{\partial^2 u_D}{\partial \theta^2} \right) \right. \\ &+ 2(1-\nu_D) \left[\frac{\partial}{\partial r} \left(\frac{1}{r} \frac{\partial u_D}{\partial \theta} \right) \right]^2 \left. \right\} r dr d\theta \\ &+ \frac{1}{2} \int_0^{2\pi} \int_a^b \left[N_r \left(\frac{\partial u_D}{\partial r} \right)^2 + N_\theta \left(\frac{1}{r} \frac{\partial u_D}{\partial \theta} \right)^2 \right] r dr d\theta.\end{aligned}\quad (13)$$

For elastic support in the rotor system, it can be calculated by the principle of virtual work. The formula is shown as follows:

$$\delta W(t) = - \sum_{i=1}^N [k_1(v_s \delta v_s + w_s \delta w_s) + k_2(w_s \delta v_s - v_s \delta w_s)] \Big|_{x=bi}.\quad (14)$$

The elastic disk-shaft rotor is approximately analyzed by the modal synthesis method. Ritz base of each substructure is obtained with the subsystem hypothesis morphological method. Eigenfunctions of transverse vibrations from flexible beam and shear beam with free ends are selected as the hypothetical function of continuous shaft transverse deflection induced by bending and shearing. Free vibration eigenfunction of the balanced disk is applied as the hypothesis function of the elastic disk in the system.

Transverse deformation of the elastic disk is expressed as

$$\begin{aligned}R_{1n}(r) &= A_n J_1 \left(\frac{\beta_n r}{b} \right) + B_n Y_1 \left(\frac{\beta_n r}{b} \right) \\ &+ C_n I_1 \left(\frac{\beta_n r}{b} \right) + D_n K_1 \left(\frac{\beta_n r}{b} \right), \quad n = 0, 1, 2, \dots,\end{aligned}\quad (15)$$

where corner marker "1" indicates the first section diameter mode, corner marker "n" indicates the number of pitch circles (not including pitch circle subjected to the inner circle clamp). J_1 and Y_1 are the Bessel functions of the first and second types, respectively, and I_1 and K_1 are the improved Bessel functions of the first and second types, respectively. A_n , B_n , C_n , and D_n are the constants which are determined by boundary conditions, the number of pitch circles, and the condition of orthogonality. β_n is the dimensionless parameter related to natural frequency ω_n , and the relation is expressed as

$$\beta_n^4 = \omega_n^2 \rho_D h_D b^4 / D.\quad (16)$$

Coefficient matrix determinant of linear equations is zero by the boundary conditions, so β_n can be obtained.

According to the Lagrange equation:

$$\frac{d}{dt} \left(\frac{\partial L}{\partial \dot{q}_i} \right) - \frac{\partial L}{\partial q_i} = 0,\quad (17)$$

where $L = T_s + T_D - V_s - V_D$, and the following is obtained:

$$\mathbf{M}\ddot{\mathbf{q}} + \mathbf{C}\dot{\mathbf{q}} + \mathbf{G}\dot{\mathbf{q}} + \mathbf{K}\mathbf{q} = 0.\quad (18)$$

As can be seen from Figure 2, each boundary or connection condition is shown as follows.

The boundary condition of O point is expressed as

$$\begin{aligned}\mu_1 G_1 A_1 (\Theta_1 - f_1') \Big|_{x_1=0} &= m_D \omega^2 f_1 \Big|_{x_1=0}, \\ -E_1 I_1 \Theta_1' \Big|_{x_1=0} &= (J_{d1} \omega^2 \Theta_1 - J_{p1} \Omega \omega \Theta_1) \Big|_{x_1=0}.\end{aligned}\quad (19)$$

Connection condition of A point is expressed as

$$\begin{aligned} \mu_1 G_1 A_1 (\Theta_1 - f_1') \Big|_{x_1=l_1} - \mu_2 G_2 A_2 (\Theta_2 - f_2') \Big|_{x_2=0} &= k_1 f_2 \Big|_{x_2=0}, \\ \frac{\partial \Theta_1}{\partial x_1} \Big|_{x_1=l_1} &= \frac{\partial \Theta_2}{\partial x_2} \Big|_{x_2=0}, \\ f_1 \Big|_{x_1=l_1} &= f_2 \Big|_{x_2=0}, \\ \Theta_1 \Big|_{x_1=l_1} &= \Theta_2 \Big|_{x_2=0}. \end{aligned} \quad (20)$$

The boundary condition of B point is expressed as

$$\begin{aligned} \mu_2 G_2 A_2 (\Theta_2 - f_2') \Big|_{x_2=l_2} - \mu_3 G_3 A_3 (\Theta_3 - f_3') \Big|_{x_3=0} &= k_2 f_3 \Big|_{x_3=0}, \\ \frac{\partial \Theta_2}{\partial x_2} \Big|_{x_2=l_2} &= \frac{\partial \Theta_3}{\partial x_3} \Big|_{x_3=0}, \\ f_2 \Big|_{x_2=l_2} &= f_3 \Big|_{x_3=0}, \\ \Theta_2 \Big|_{x_2=l_2} &= \Theta_3 \Big|_{x_3=0}. \end{aligned} \quad (21)$$

The boundary condition of free end is expressed as

$$\begin{aligned} \frac{\partial \Theta_3}{\partial x_3} \Big|_{x_3=l_3} &= 0, \\ \left[\Theta_3 - \frac{\partial f_3}{\partial x_3} \right] \Big|_{x_3=l_3} &= 0. \end{aligned} \quad (22)$$

By solving the equation set formed by the above equations, natural frequency and mode shape of the system can be obtained.

3.2. Differential Equations of Rotor System under Airflow Excitation Force. In order to analyze the effect of Alford force on rotor stability, the equivalent cross stiffness is applied to indicate the action of Alford force. Figure 3 illustrates the process of instability caused by equivalent cross stiffness. O point represents the axis before the deformation, and O' point represents the axis after deformation. R is the the radius of casing, and δ is the clearance between rotor and casing. Assuming that the rotor is precessing by the effect of unbalance, the direction of precession is shown by the arrow in Figure 3. F_c is the inertia force, F_e is the elastic recovery force, F_d is the external damping force, and F_a is induced by the Alford force. If F_a is greater than the force of outer damping F_d on the turbine, it will accelerate the positive precession. So the inertial force increases, the deflection increases, the unstable force increases, and the precession is faster. With this development, vibration amplitude of self-energized motion increases until it is limited by the structure or reaches the limit circle (or has caused damage before).

By the action of rotational dragging, the fluid will generate a circular flow in the sealing gap, which plays a significant role in rotor vibration. In a certain conditions, it will cause the rotor instable and generate self-excited

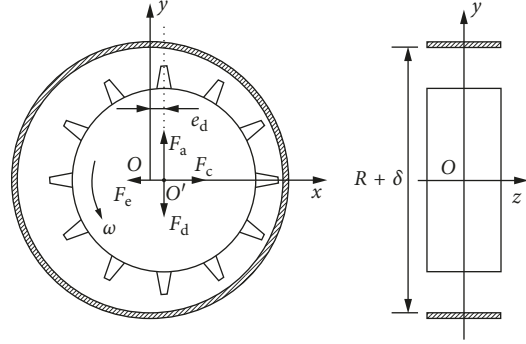


FIGURE 3: The model of rotor damage-instability caused by aerodynamic excitation force.

lateral vibration. In 1987, Muszynska and Bently [23] proposed the Muszynska model based on a large number of experiments. This model introduces the average circumferential speed ratio τ to characterize the overall motion of fluid in the gap between the bearing and sealing. Rotational effect of seal excitation force is the main factor of rotor instability. The reaction force caused by sealing excitation force rotates around the rotor at a fixed angular velocity. In fixed coordinates, this reaction force can be described as the following mathematical equation:

$$\begin{aligned} - \begin{bmatrix} F_x \\ F_y \end{bmatrix} &= \begin{bmatrix} K - m_f \tau^2 \omega^2 & \tau \omega D \\ -\tau \omega D & K - m_f \tau^2 \omega^2 \end{bmatrix} \begin{bmatrix} x \\ y \end{bmatrix} \\ &+ \begin{bmatrix} D & 2\tau m_f \omega \\ -2\tau m_f \omega & D \end{bmatrix} \begin{bmatrix} \dot{x} \\ \dot{y} \end{bmatrix} + \begin{bmatrix} m_f & \\ & m_f \end{bmatrix} \begin{bmatrix} \ddot{x} \\ \ddot{y} \end{bmatrix}. \end{aligned} \quad (23)$$

where K , D , and m_f indicate the stiffness, damping, and inertia effects of fluid's disturbing motion on the rotor. It is generally taken that cyclic force is rotor tangential driving force constituted by the cross stiffness term $\tau \omega D$. According to the equation, larger fluid damping D is easy to make rotor instable. Reducing the average circumferential velocity ratio τ can improve the stability of the rotor-seal system. A large number of experiments [24] have proved the assertion that the application of antiswirling structure can improve the stability of the sealing system. In addition, the main stiffness term in the model, that is, rotor radial stiffness $K - m_f \tau^2 \omega^2$, can become a negative value at the effect of fluid centrifugal inertia force.

Perturbation analysis and experimental data show that [25] the effect of fluid centrifugal inertia force becomes very obvious, when the ratio of seal gap and rotor radius is small. This has a great influence on the stiffness matrix. So the radial stiffness term can easily reach a negative value, and it is also a factor that causes rotor instable. The Muszynska model correctly reflects the basic dynamic characteristics of sealing force. Equation (23) not only is applied in the condition of small displacement at the rotor center position but also can indicate the nonlinear sealing force at larger displacement. Experimental and numerical results confirm that [26] τ , K , and D are the nonlinear

functions of disturbed displacements x and y . It can be expressed as follows:

$$\begin{aligned} K &= K_0(1 - e^2)^{-n}, \\ D &= D_0(1 - e^2)^{-n}, \\ n &= \frac{1}{2} \sim 3, \\ \tau &= \tau_0(1 - e^2)^b, \quad 0 < b < 1. \end{aligned} \quad (24)$$

where $e = (\sqrt{x^2 + y^2}/C_r)$ is rotor relative partial displacement and C_r is the sealing clearance. Specific seal is approximately described by selecting the appropriate exponents n and b . Due to the effects of axial flow, surface roughness, secondary flow, and other factors, in general $\tau_0 < (1/2)$. K_0 , D_0 , and m_f can be calculated by the combination of Childs seal dynamic coefficient equation and equation (24):

$$\begin{aligned} K_0 &= \mu_3 \mu_0, \\ D_0 &= \mu_1 \mu_3 T, \\ m_f &= \mu_2 \mu_3 T^2. \end{aligned} \quad (25)$$

The Muszynska sealing force model is mainly based on a large number of experiments and abstracted from the model. It has a strong generality and grasps the main mechanical characteristics of sealing force. The correctness of the Muszynska model has been widely recognized in the application. The Muszynska sealing force model is adopted as the model of airflow excitation force, and the dynamic differential equation of the elastic disc-flexible shaft rotor is established by the modal synthesis method.

Applying the principle of virtual work, virtual work caused by the Alford force can be obtained as

$$\begin{aligned} \delta W(t) &= -[k_1(v_s \delta v_s + w_s \delta w_s) + k_2(w_s \delta v_s - v_s \delta w_s) \\ &\quad + c_1(\dot{v}_s \delta v_s + \dot{w}_s \delta w_s) + c_2(\dot{w}_s \delta v_s - \dot{v}_s \delta w_s) \\ &\quad - c_1 \Omega(w_s \delta v_s - v_s \delta w_s) + c_2 \Omega(v_s \delta v_s - w_s \delta w_s) m_f \\ &\quad \cdot (\ddot{v}_s \delta v_s + \ddot{w}_s \delta w_s) + m_f \Omega(\dot{w}_s \delta v_s - \dot{v}_s \delta w_s) \\ &\quad + m_f \Omega^2(v_s \delta v_s + w_s \delta w_s)] \delta, \end{aligned} \quad (26)$$

where

$$\begin{aligned} k_1 &= K - m_f \tau^2 \omega^2, \\ k_2 &= \tau \omega D, \\ c_1 &= D, \\ c_2 &= 2\tau m_f \omega. \end{aligned} \quad (27)$$

According to the modal synthesis method, the dynamic equation of the rotor can be expressed as

$$\mathbf{M}\ddot{\mathbf{q}} + \mathbf{C}\dot{\mathbf{q}} + \mathbf{G}\dot{\mathbf{q}} + \mathbf{K}\mathbf{q} = \mathbf{F}_q + e\Omega^2 \mathbf{F}_e. \quad (28)$$

where \mathbf{F}_e is the imbalance force caused by eccentric mass and \mathbf{F}_q is the force of bearing oil film. \mathbf{F}_q is expressed as

$$\mathbf{F}_q = -(\mathbf{K}_q \mathbf{q} + \mathbf{C}_q \dot{\mathbf{q}} + \mathbf{G}_q \dot{\mathbf{q}} + \mathbf{M}_q \ddot{\mathbf{q}}), \quad (29)$$

where

$$\mathbf{\Phi} = \begin{bmatrix} \mathbf{\Phi}_{s1}^T |_d \mathbf{\Phi}_{s1} |_d & \mathbf{\Phi}_{s1}^T |_d \mathbf{\Phi}_{s2} |_d \\ \mathbf{\Phi}_{s2}^T |_d \mathbf{\Phi}_{s1} |_d & \mathbf{\Phi}_{s2}^T |_d \mathbf{\Phi}_{s2} |_d \\ & & 0 \end{bmatrix}. \quad (30)$$

So \mathbf{K}_q , \mathbf{C}_q , \mathbf{G}_q , and \mathbf{M}_q in equation (29) are expressed as

$$\begin{aligned} \mathbf{K}_q &= \begin{bmatrix} \mathbf{K}_{q1} & \mathbf{K}_{q2} \\ -\mathbf{K}_{q2}^T & \mathbf{K}_{q1} \end{bmatrix}, \\ \mathbf{K}_{q1} &= (k_1 + c_2 \Omega + m_f \Omega^2) \mathbf{\Phi}, \\ \mathbf{K}_{q2} &= (k_2 + c_1 \Omega) \mathbf{\Phi} \\ \mathbf{C}_q &= \begin{bmatrix} \mathbf{C}_{q1} & \mathbf{C}_{q2} \\ -\mathbf{C}_{q2}^T & \mathbf{C}_{q1} \end{bmatrix}, \\ \mathbf{C}_{q1} &= c_1 \mathbf{\Phi}, \\ \mathbf{C}_{q2} &= c_2 \mathbf{\Phi}, \\ \mathbf{G}_q &= \begin{bmatrix} & \mathbf{G}_{q1} \\ -\mathbf{G}_{q1}^T & \end{bmatrix}, \\ \mathbf{G}_{q1} &= m_f \Omega \mathbf{\Phi}. \end{aligned} \quad (31)$$

Assuming that $\bar{q} = q/C_r$, $\dot{\bar{q}} = (d\bar{q}/d\tau)(d\tau/dt) = \Omega \bar{q}'$, and $\bar{e} = e/C_r$, equation (28) is expressed as

$$(\mathbf{M} + \mathbf{M}_q) \bar{q}'' + \frac{(\mathbf{C} + \mathbf{C}_q)}{\Omega} \bar{q}' + \frac{(\mathbf{G} + \mathbf{G}_q)}{\Omega} \bar{q}' + \frac{(\mathbf{K} + \mathbf{K}_q)}{\Omega^2} \bar{q} = \bar{e} \mathbf{F}_e. \quad (32)$$

4. Analysis and Discussion of the Results

In order to explain the effects of different parameters on rotor vibration responses, rotor parameters are taken as follows if no special description is given. The geometric parameters of rotor structure are indicated as $l_1 = 0.35$, $l_2 = 0.95$ m, and $l_3 = 0.65$ m. The inner and outer radii, thickness, density, elastic modulus, and Poisson's ratio of the elastic disk are, respectively, indicated as $a = 0.11$ m, $b = 0.445$ m, $h_D = 0.088$ m, $\rho_D = 4640$ kg/m³, $E_D = 1.13 \times 10^{11}$ N/m², and $\nu_D = 0.28$. The radius, density, Poisson's ratio, and elastic modulus of the flexible shaft are indicated as $r_s = 0.11$ m, $\rho_s = 7900$ kg/m³, $\nu_s = 0.28$, and $E_s = 2.06 \times 10^{11}$ N/m². The stiffness coefficient of elastic support is indicated as $k_{11} = k_{21} = 6.0 \times 10^8$ N/m. The damping coefficient of the support is indicated as $c_{11} = c_{21} = 3000$ N · s/m.

In the model of aerodynamic excitation force, the circumferential loss coefficient of sealed inlet airflow is indicated as $\xi = 0.1$. The seal length is indicated as $l = 0.088$. The radial seal clearance is indicated as $\delta = 2$ mm. Fluid average axial velocity in the sealing cavity is indicated as $v = 5$ m/s. The sealing radius is indicated as $R = 0.445$ m. The coefficient of fluid viscosity is indicated as $\mu = 1.8 \times 10^{-5}$ pa · s. The empirical coefficients are indicated

as $m_0 = -0.25$, $n_0 = 0.079$, $\tau_0 = 0.25$, and $n = 2$. Axial seal pressure drop is indicated as $\Delta P = (\rho v^2 (1 + \xi + 2\delta))/2$, where ρ is the density of gas.

4.1. Natural Vibration Analysis of Flexible Shaft and Elastic Disk Rotor

4.1.1. Comparison of Results at Different Modes. Take the shaft bending mode number, shaft shear mode number, and the disk modal number are, respectively, as 25, 25, and 4. The first eight natural frequencies of the rigid disk-flexible shaft rotor system can be obtained based on the boundary and connection conditions. Similarly, the first eight natural frequencies of the elastic disk-flexible shaft rotor system can be obtained, as shown in Table 1.

The corresponding mode shapes are shown in Figure 4.

From modal vibration shapes in Figures 4(a) and 4(b), it can be seen that the vibration of the disk is not obvious at the low-order frequency. As the frequency increases, the vibration of the disk gradually becomes prominent.

The above derivation is performed in the rotating coordinate of shaft and the rotating coordinate of the disc, so the obtained natural frequencies are also relative to the rotating coordinate system. In order to compare with the experimental data, it is necessary to convert the obtained natural frequency into an inertial coordinate system. For the transverse vibration of the shaft and disk, the conversion relationship is different between rotating coordinate system and inertial coordinate system. Hence, there are two different natural frequencies in the inertial coordinate system.

4.1.2. Analysis of Coupled Natural Frequency in Transverse Vibration. For transverse vibration of the shaft, conversion relation is expressed as

$$\omega_0 = \omega + \Omega, \quad (33)$$

where ω is the natural frequency in the rotating coordinate system, Ω is the angular velocity of the shaft, and ω_0 is the natural frequency in the inertial coordinate system.

For transverse vibration of the disk, the transformation is difficult from the rotating coordinate system to the inertial coordinate system. Compared with the rotation angle Ωt , declination angles θ_ξ and θ_η of transverse vibration can be ignored in the transformation of the coordinate system. So, the relationship between two angular coordinate systems can be expressed as

$$\theta_0 = \theta + \Omega t. \quad (34)$$

Excitation force of the disc is $F_0 \cos \omega_0 t$, and vibration response at $r_0 = \rho$ and $\theta_0 = 0$ is expressed as

$$u = K(\rho, m) F_0 f(r) \cos m\theta \left[\frac{\cos(\omega_0 + m\Omega)t}{|\omega^2 - (\omega_0 + m\Omega)^2|} + \frac{\cos(\omega_0 - m\Omega)t}{|\omega^2 - (\omega_0 - m\Omega)^2|} \right], \quad (35)$$

where ω is the natural frequency in the rotating coordinate system and m is the number of mode nodal diameters in

the disk. It can be seen from the above equation that there are two resonant frequencies in the inertial coordinate system:

$$\omega_0 = \omega + m\Omega, \quad \omega_0 = \begin{cases} \omega - m\Omega, & \omega \geq m\Omega, \\ -(\omega - m\Omega), & \omega < m\Omega. \end{cases} \quad (36)$$

Plotting the chart of frequency-rotational angular velocity, $\omega - m\Omega$ and $-(\omega - m\Omega)$ are the continuous curves. Therefore, natural frequencies are generally divided into two parts when rotating. That is, at a certain rotational angular velocity, two different excitation frequencies will excite the same response mode in the inertial space.

For the specific problem, natural frequency of disk-shaft coupling is indicated as ω . The antiprecession mode of the rotating system may be negative, and only the first nodal diameter mode of the disk will couple with the vibration of shaft, so $m = 1$. Equation (36) can be expressed as

$$\omega_0 = |\omega| + \Omega, \quad \omega_0 = \begin{cases} |\omega| - \Omega, & \omega \geq m\Omega, \\ -(|\omega| - \Omega), & \omega < m\Omega. \end{cases} \quad (37)$$

According to equation (28), the coupled natural frequency of shaft transverse vibration is shown as Figure 5. Here, 5(a) is the diagram of coupled natural frequency in the flexible shaft and rigid disk, and 5(b) is the diagram of coupled natural frequency in the flexible shaft and elastic disk.

In Figure 5, the difference between Figures 5(a) and 5(b) is obvious when the rotational speed is large, and the difference between two models is smaller in the region with lower rotational speed. It is illustrated that modal vibration of the shaft occupies a dominant position in the low rotational speed region. Modal vibration of the disk has little effect on the coupled natural frequency of shaft transverse vibration, while it takes a great effect in the high rotational speed region. Hence, the difference between two models is quite obvious.

According to equation (37), the coupled natural frequency of elastic disk transverse vibration is shown as Figure 6. Here, 6(a) is the diagram of forward natural frequency, and 6(b) is the diagram of backward natural frequency.

Mass matrix and stiffness matrix of the rotor system will be affected by the coupling effect of shaft and disk, but the gyroscopic matrix and damping matrix are not affected. Without considering the physical background, the disk-shaft coupling term can be directly removed in the mass matrix and stiffness matrix. So, it is to analyze the effect of the disk-shaft coupling on rotor natural frequency.

From Figure 7, it can be seen that the effect of shaft-disk coupling makes rotor frequency decrease, and different rotational speeds have little effect on rotor frequency.

The effects of different structural parameters are discussed on rotor frequency. Figure 8(a) shows the frequency of the rotor system decreases with the increase of outer diameter. From Figure 8(b), the first-order frequency of the rotor system decreases when the first support moves to the right, but the third-order frequency increases.

TABLE 1: First eight natural frequencies of the rigid disk and elastic disk rotor models.

Frequency ($\text{rad}\cdot\text{s}^{-1}$)	ω_1	ω_2	ω_3	ω_4	ω_5	ω_6	ω_7	ω_8
Rigid disk rotor	701.26	931.53	1491.22	2879.45	4918.80	8051.80	11967.90	16246.80
Elastic disk rotor	700.51	931.04	1474.40	2585.82	4553.73	7546.20	11250.92	15203.63

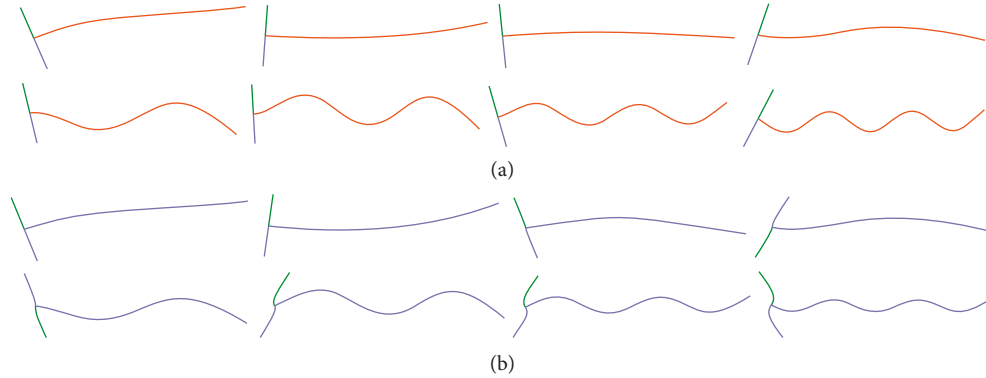


FIGURE 4: Mode shape comparison of the different rotor models: first eight mode shapes of (a) flexible shaft and rigid disk rotor system and (b) flexible shaft and elastic disk rotor system.

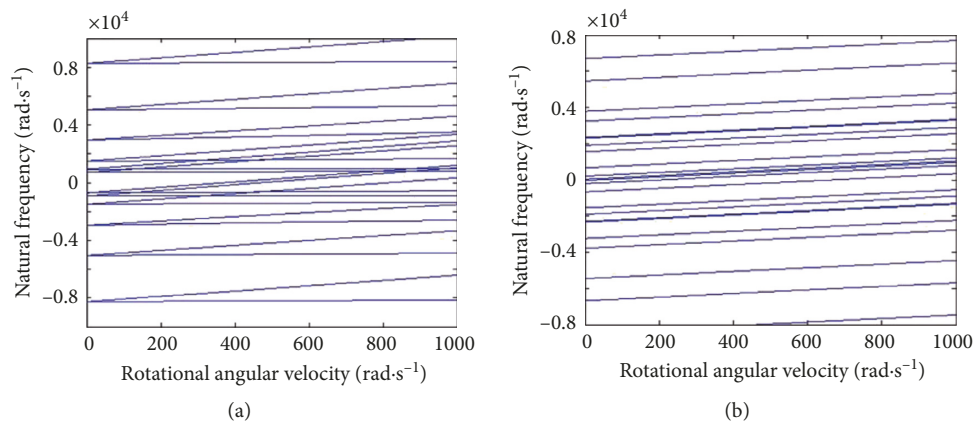


FIGURE 5: Coupled natural frequency of the shaft transverse vibration: (a) flexible shaft and rigid disk system and (b) flexible shaft and elastic disk system.

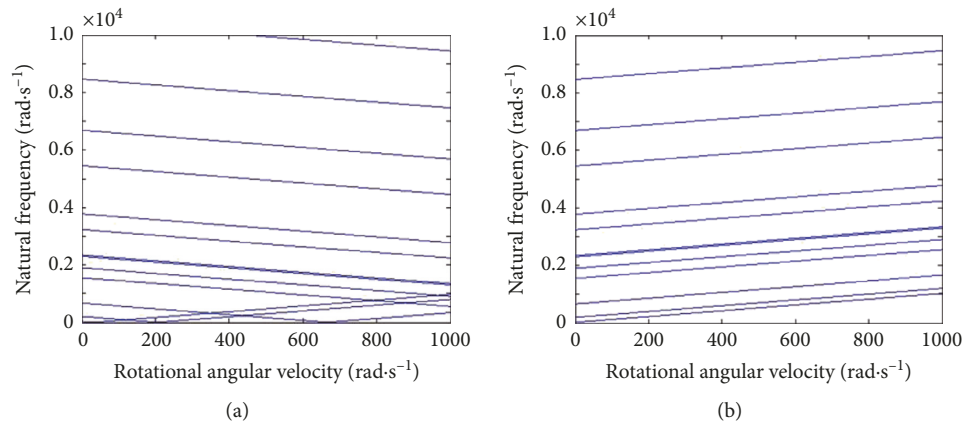


FIGURE 6: Coupled natural frequency of transverse vibration of the disk: (a) forward precessional modes and (b) backward precessional modes.

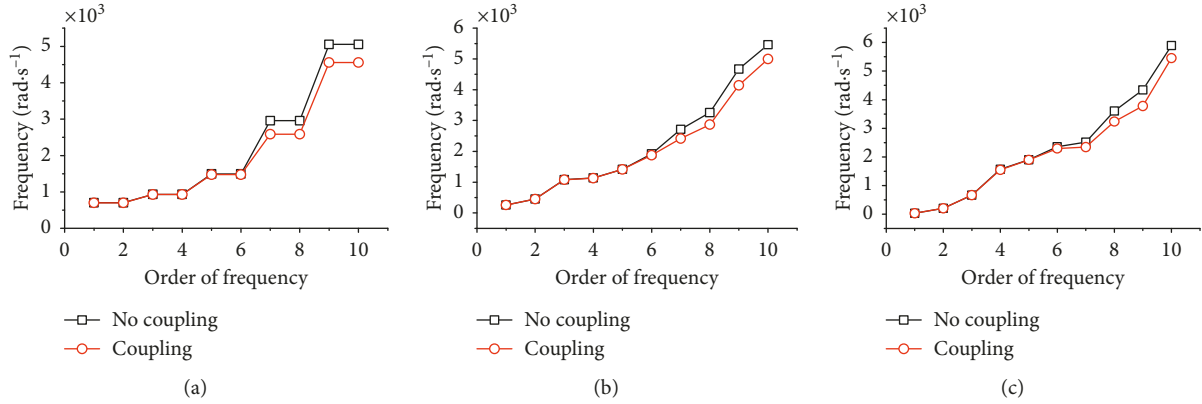


FIGURE 7: The effect of disk-shaft coupling term on rotor natural frequency: (a) $\Omega = 0$ rad/s, (b) $\Omega = 500$ rad/s, and (c) $\Omega = 1000$ rad/s.

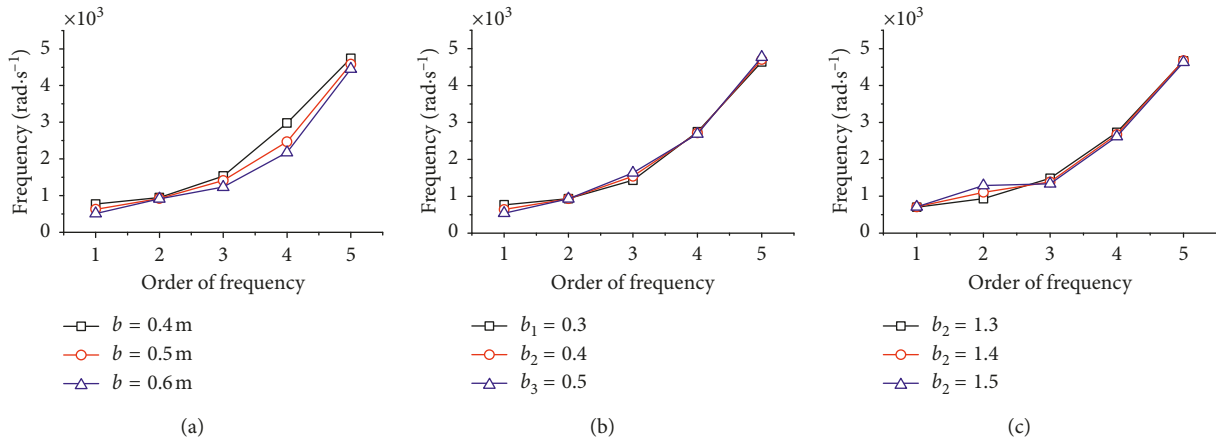


FIGURE 8: The effect of structure parameters on rotor natural frequency: (a) radius of the disk, (b) position of the first support, and (c) position of the second support.

In Figure 8(c), the second-order frequency of the rotor system decreases obviously when the second support moves to the right, and it has little effect on the frequencies of other orders.

4.2. Stability Analysis of Elastic Disk-Flexible Shaft at Aerodynamic Force. The effects of different parameters are discussed on rotor time-domain chart, axis orbit, and spectrum graph. Based on the variation of rotor responses, the stability of rotor system is analyzed. Here, the dimensionless displacement in the y direction is denoted as Y , the dimensionless displacement in the z direction is denoted as Z , the ratio of average circumferential speed is denoted as τ , the frequency of rotor response is denoted as f , and the amplitude of rotor response is denoted as A .

4.2.1. The Effect of Eccentric Distance and Rotational Speed. Figures 9 and 10 show the responses of the rotor system at different imbalance and rotational speed. According to the spectrum graph, the responses of the rotor system include the frequencies caused by aerodynamic excitation force and

rotor imbalance. Summarizing the above figures, rotor frequency caused by aerodynamic excitation force can be obtained, and it is about 50 Hz.

Comparing with rotor responses at different eccentric distances, there is no clear change in rotor motion law and relative relationship between two response frequencies. It illustrates eccentric distance has little effect on rotor stability, and only the amplitude of rotor response is changed.

With the increase of rotational speed, the value of vibration frequency caused by the imbalance increases, and the proportion of vibration response caused by aerodynamic excitation force becomes larger. Ultimately, the rotor system is caused unstable when rotational speed increases to be a certain value.

4.2.2. The Effect of Disk Radius. Figure 11 shows the responses of the rotor system at different disk radii. According to spectrum graphs, the proportion of rotor responses caused by aerodynamic excitation force becomes larger with the increase in the disk radius and gradually covers the response caused by the imbalance. Comparing with the

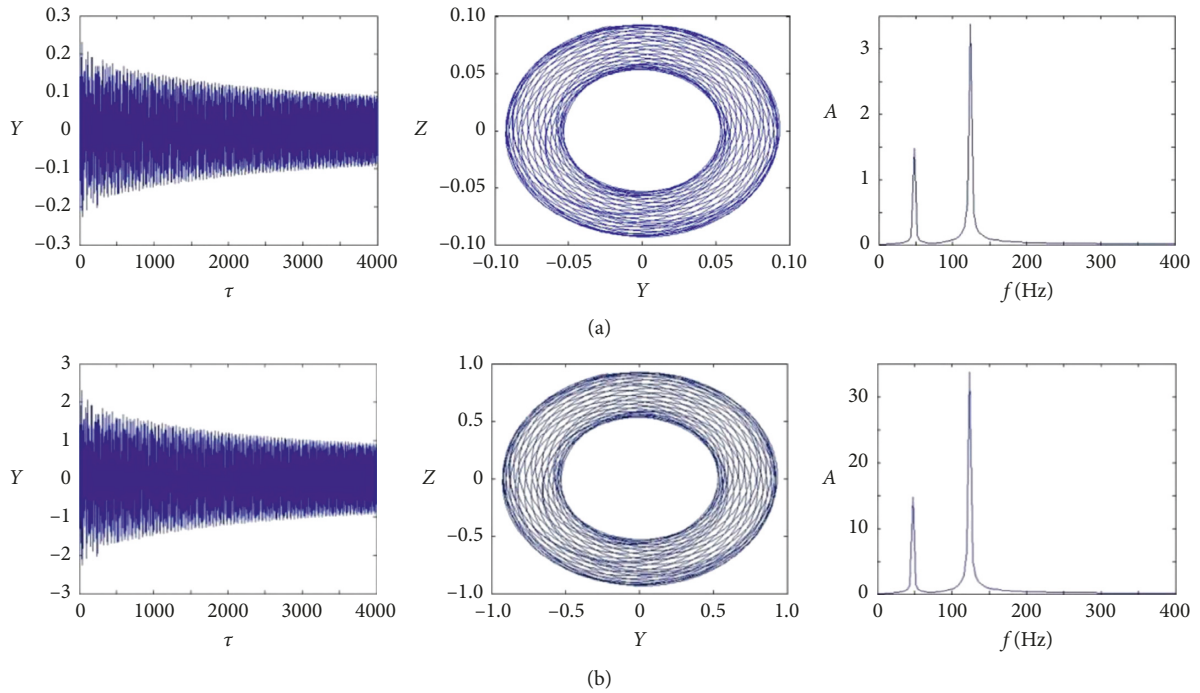


FIGURE 9: Rotor responses of the time domain, axis orbit, and spectrum at eccentric distances $\bar{e} = 0.001$ (a) and $\bar{e} = 0.01$ (b) and rotational speed $\Omega = 800$ rad/s.

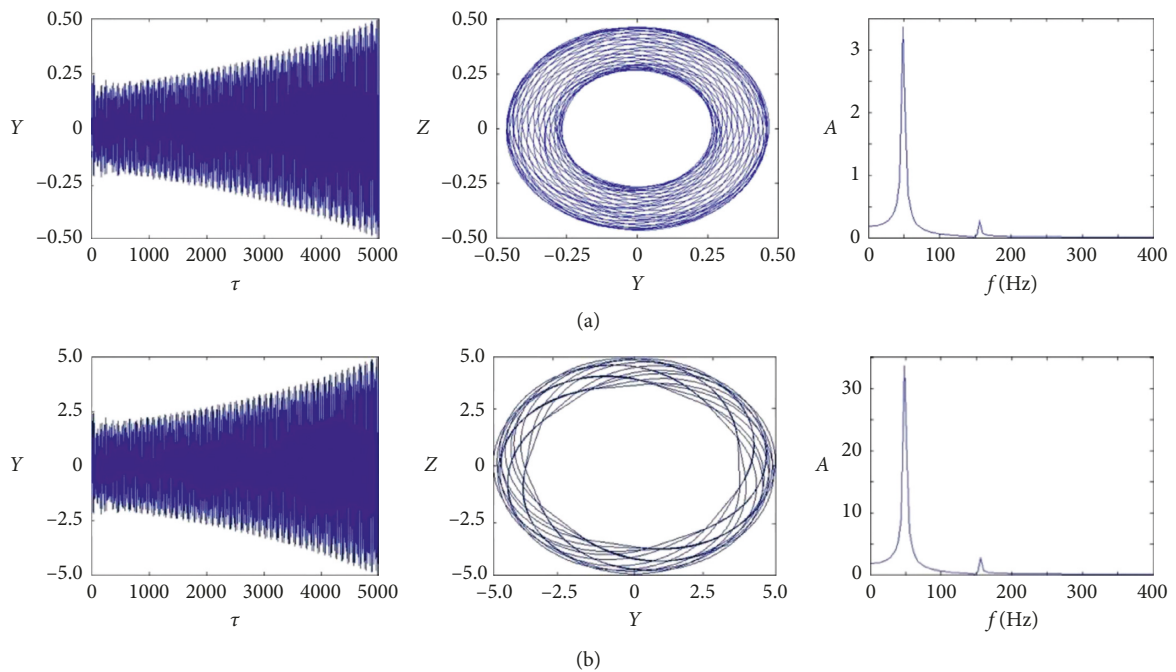


FIGURE 10: Rotor responses of time domain, axis orbit, and spectrum at eccentric distances $\bar{e} = 0.001$ (a) and $\bar{e} = 0.01$ (b) and rotational speed $\Omega = 1000$ rad/s.

charts of the time domain, vibration amplitude of the rotor system increases rapidly with the increase in the disk radius. The rotor system becomes unstable when the disk radius increases to be a certain value.

4.2.3. *The Effect of Support Position.* Figure 12 shows the responses of the rotor system at different positions of the second support. According to spectrum graphs, the proportion of rotor responses caused by aerodynamic

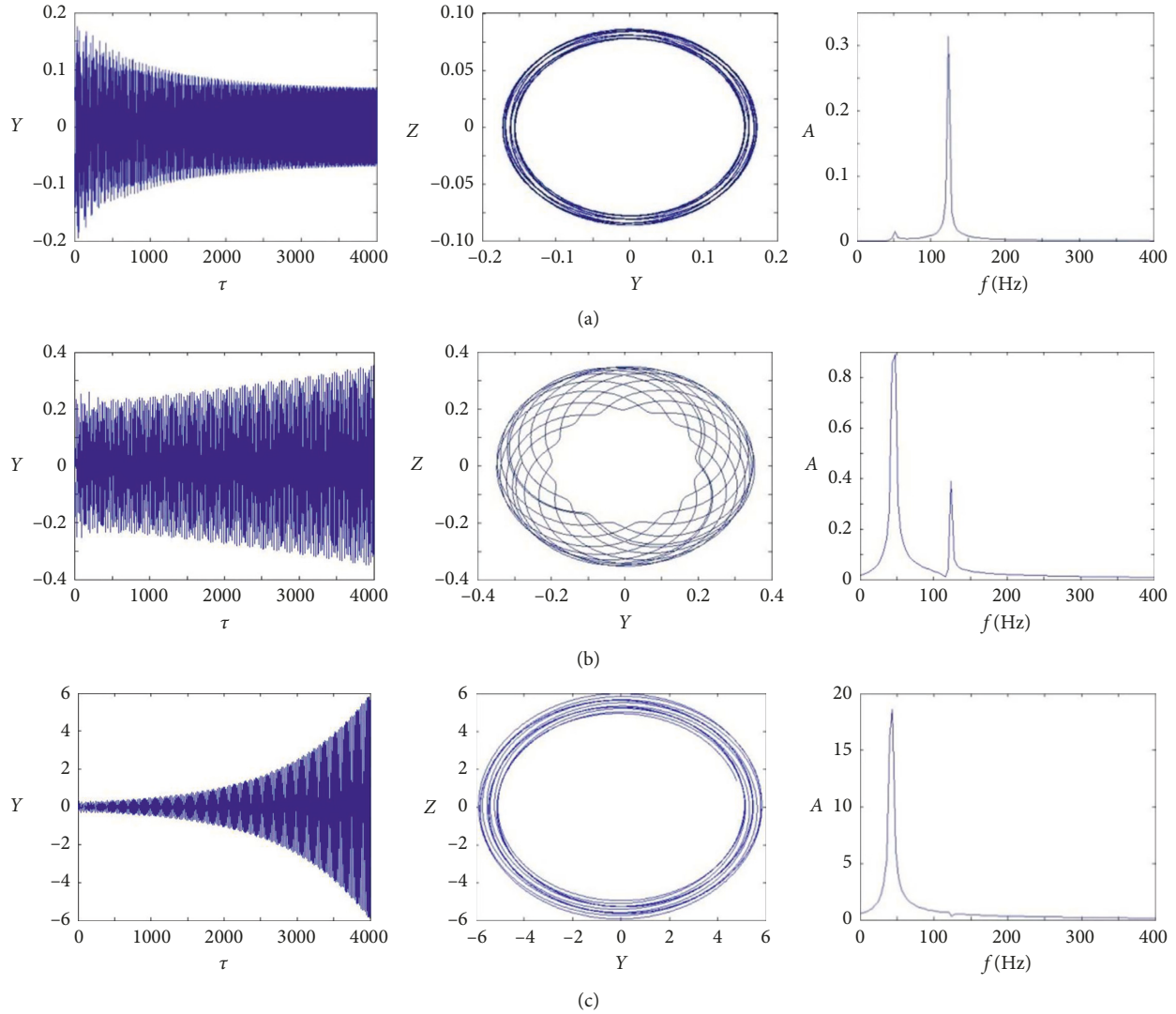


FIGURE 11: Rotor responses of time domain, axis orbit, and spectrum at different disk radii. (a) $b = 0.4$ m, (b) $b = 0.5$ m, and (c) $b = 0.6$ m.

excitation force decreases with the second support moving to the right. Comparing with the charts of the time domain, vibration amplitude of the rotor system becomes smaller rapidly with the second support moving to the right. It is because that support center of the whole rotor system is also moving to the right; the mass of disk and Alford force can be balanced. The rotor system would be stable when the second support moves to the right at a certain position.

5. Conclusions

Vibration differential equations of the elastic disk-flexible shaft rotor are established by the modal synthesis method. Based on the Runge-Kutta method of direct integration, vibration characteristics of the elastic disk and the flexible shaft rotor were analyzed successfully. Then, the effects of Alford force caused by the airflow excitation are further researched on the stability and dynamic response. The results show the following:

- (1) Comparing with vibration characteristics of different rotor models, modal vibration of the disk takes a great effect on the coupled natural frequency of shaft transverse vibration in the high rotational speed region. The effect of shaft-disk coupling makes rotor frequency decrease, and different rotational speeds have little effect on rotor frequency. The frequency of the rotor system decreases with the increase in outer diameter. The first-order frequency decreases with the first support moving to the right, but the third-order frequency increases. When the second support moves to the right, the second-order frequency of the rotor system decreases obviously.
- (2) Analysis of rotor responses at different structure parameters was performed, and eccentric distance is sensitive to the amplitude of rotor response, but it has little effect on rotor stability, motion law, and relative relationship of two response frequencies. The proportion of rotor responses caused by aerodynamic excitation force becomes larger with the

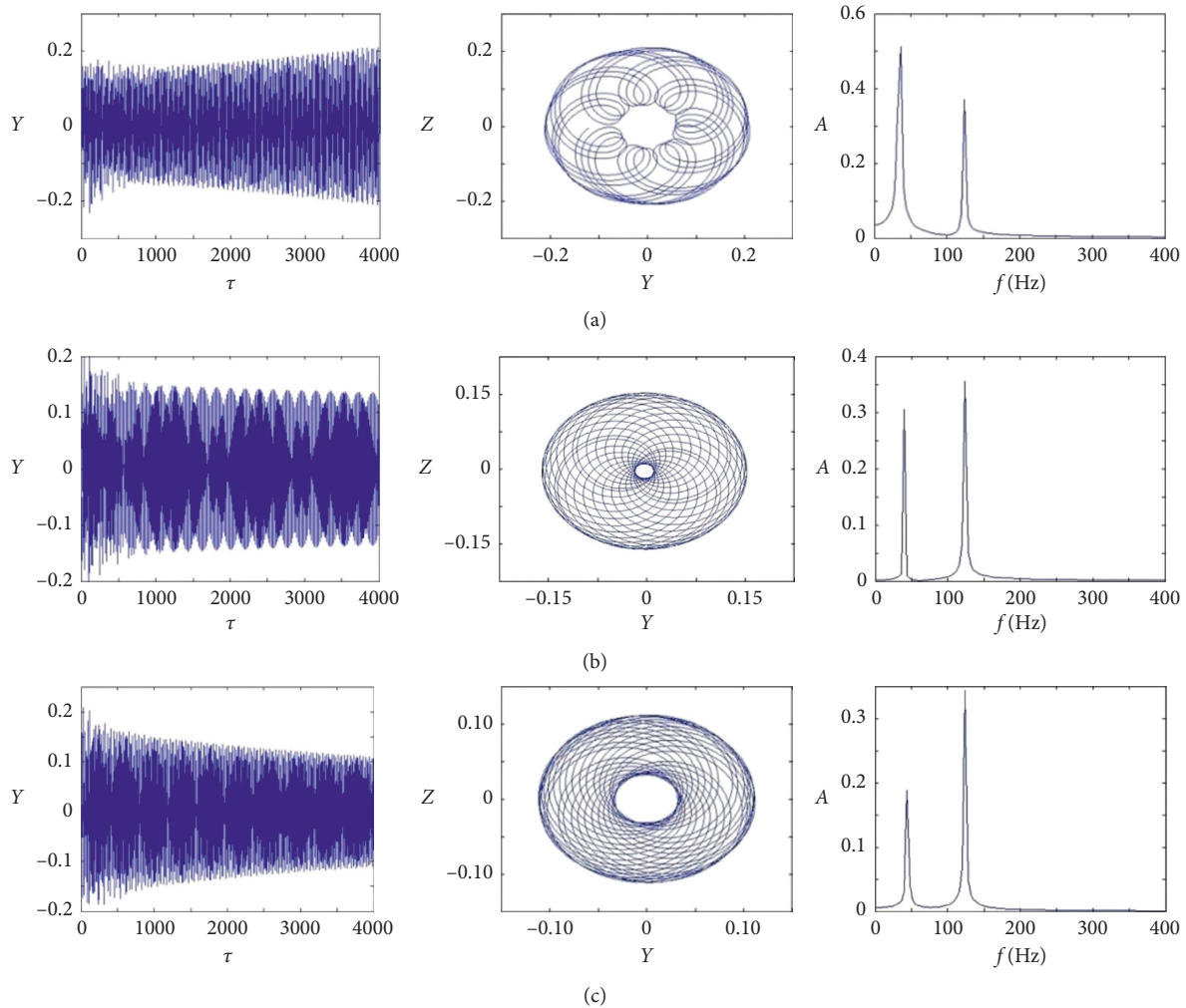


FIGURE 12: Rotor responses of time domain, axis orbit, and spectrum at different second support positions. (a) $l_2 = 1.0$ m, (b) $l_2 = 1.1$ m, and (c) $l_2 = 1.2$ m.

increase of rotational speed and disk radius. The rotor system becomes unstable when rotational speed or disk radius increases to a certain value. However, the proportion decreases with the second support moving to the right, and it is helpful for the stable operation of the rotor system.

Data Availability

The data used to support the findings of this study are available from the corresponding author upon request.

Conflicts of Interest

The authors declare that they have no conflicts of interest.

Acknowledgments

The work was supported by the Natural Science Foundation of Liaoning Province (Grant no. 20180550880), Education Department Series Project of Liaoning Province (Grant no.

L201746), and Young Doctor Scientific Research Foundation of College (Grant no. 17YB04).

References

- [1] S. H. Gao and G. Meng, "Research of the spindle overhang and bearing span on the system milling stability," *Archive of Applied Mechanics*, vol. 81, no. 10, pp. 1473–1486, 2010.
- [2] F. Han, X. L. Guo, and H. Y. Gao, "Research on coupled bending and torsion vibration of blade-rotor-bearing system with nonlinear oil-film force," *Engineering Mechanics*, vol. 30, no. 4, pp. 355–359, 2013.
- [3] W. Zhang, *Basis of Rotor Dynamics*, Scientific Press, Beijing, China, 1990.
- [4] J. L. Meek and H. Liu, "Nonlinear dynamics analysis of flexible beams under large overall motions and the flexible manipulator simulation," *Computers & Structures*, vol. 56, no. 1, pp. 1–14, 1995.
- [5] J. Y. Kim, S. H. Hyun, and H. H. Yoo, "Nonlinear modeling and dynamic analysis of flexible structures undergoing overall motions employing mode approximation method," *KSME International Journal*, vol. 16, no. 7, pp. 896–901, 2002.

- [6] M. A. Hili, T. Fakhfakh, and M. Haddar, "Vibration analysis of a rotating flexible shaft-disk system," *Journal of Engineering Mathematics*, vol. 57, no. 4, pp. 351–363, 2006.
- [7] H. Yeo, M. Potsdam, and R. A. Ormiston, "Rotor aeroelastic stability analysis using coupled computational fluid dynamics/computational structural dynamics," *Journal of the American Helicopter Society*, vol. 56, no. 56, pp. 1–16, 2011.
- [8] X. H. Jiang and Y. R. Wang, "Numerical simulation of bird impact on bladed rotor stage by fluid-solid coupling method," *Journal of Aerospace Power*, vol. 23, no. 2, pp. 299–304, 2008.
- [9] J. S. Alford, "Protecting turbo-machinery from self-excited rotor whirl," *Journal of Engineering for Power*, vol. 87, no. 10, pp. 333–344, 1965.
- [10] Z. S. Spakovszky, "Analysis of aerodynamically induced whirling forces in axial flow compressors," *Journal of Turbomachinery*, vol. 122, no. 4, pp. 761–768, 2000.
- [11] H. J. Thomas, "Unstable natural vibration of turbine rotors induced by the clearance flow in glands and blading," *Bull De L'AIM*, vol. 71, no. 11, pp. 1039–1063, 1958.
- [12] K. Urlichs, "Clearance flow-generated transverse forces at the rotors of thermal turbomachines," Ph. D. thesis, Technische Universität Darmstadt, Darmstadt, Germany, 1983.
- [13] R. Wohlrab, "Experimental determination of gap flow-conditioned forces at turbine stages and their effect on the running stability of simple rotors," Ph.D. thesis, Technical University of Munich, Munich, Germany, 1983.
- [14] J. M. Vance and F. J. Laudadio, "Experiment measurement of Alford's force in axial-flow turbomachinery," *Journal of Engineering for Gas Turbines and Power*, vol. 106, no. 3, pp. 585–590, 1984.
- [15] J. J. Moore, A. B. Palazzolo, and J. J. Moore, "CFD comparison to 3D laser anemometer and rotordynamic force measurements for grooved liquid annular seals," *Journal of Tribology*, vol. 121, no. 2, pp. 306–314, 1999.
- [16] D. W. Childs and J. K. Scharrer, "Experimental rotordynamic coefficient results for teeth-on-rotor and teeth-on-stator labyrinth gas seals," *Journal of Engineering for Gas Turbines and Power*, vol. 108, no. 4, pp. 599–604, 1986.
- [17] K. Y. Chien, "Predictions of channel and boundary-layer flows with a low-Reynolds-number turbulence model," *AIAA Journal*, vol. 20, no. 1, pp. 33–38, 1982.
- [18] J. Y. Shi, Q. Sun, Q. Wei et al., "Research on the steam-excited vibration of ultra supercritical steam turbines," *Power Engineering*, vol. 23, no. 5, pp. 2620–2623, 2003.
- [19] S. Chai, Y. Zhang, Q. Qu et al., "The analysis on the air-exciting-vibration force of steam turbine," *Engineering Science*, vol. 3, no. 4, pp. 68–72, 2001.
- [20] Z. Chen and Y. Sun, "The oscillating fluid mechanics method (OFMM) for studying oil film oscillation and dynamic characteristics of journal bearings," *Journal of Tribology*, vol. 118, no. 1, pp. 239–245, 1996.
- [21] Z. X. Lu, Y. B. Xie, and D. M. Qiu, "The finite-difference simulation of flow field in labyrinth seals," *Chinese Journal of Applied Mechanics*, vol. 9, no. 3, pp. 87–92, 1992.
- [22] J. G. Yang, T. Y. Zhu, and W. Gao, "Influence of steam induced vibration on stability of rotor-bearing system," *Proceedings of the CSEE*, vol. 18, no. 1, pp. 9–11, 1998.
- [23] D. E. Bently and A. Muszynska, "Role of circumferential flow in the stability of fluid-handling machine rotors," in *Proceedings of the 5th Workshop on Rotor dynamic Instability Problems in High Performance Turbo machinery*, Texas A&M University, College Station, TX, USA, May 1998.
- [24] A. Muszynska and D. E. Bently, "Anti-swirl arrangements prevent rotor/seal instability," *Journal of Vibration Acoustics Stress and Reliability in Design*, vol. 111, no. 2, pp. 156–162, 1989.
- [25] A. Muszynska and D. E. Bently, "Frequency-swept rotating input perturbation techniques and identification of the fluid force models in rotor/bearing/seal systems and fluid handling machines," *Journal of Sound and Vibration*, vol. 143, no. 1, pp. 103–124, 1990.
- [26] L. T. Tam, A. J. Przekwas, A. Muszynska et al., "Numerical and analytical study of fluid dynamic forces in seals and bearings," *Journal of Vibration & Acoustics*, vol. 110, no. 3, pp. 112–119, 1987.

